Three Dimensional Multifractal Analysis of Trabecular Bone under clinical computed tomography

Rodrigo Baravalle*

Group of Multimedia Signal Processing, CIFASIS-CONICET, Argentina

Felix Thomsen† and Claudio Delrieux‡

Imaging Sciences Lab, DIEC-CONICET,

Universidad Nacional del Sur, Bahía Blanca, Argentina

Yongtao Lu§

Department of Engineering Mechanics,

Dalian University of Technology, Dalian, China

Juan Carlos Gómez¶

Group of Multimedia Signal Processing, CIFASIS-CONICET,

Universidad Nacional de Rosario, Argentina

Borko Stošić** and Tatijana Stošić††

Department of Statistics and Informatics,

Universidade Federal Rural de Pernambuco, Recife-PE, Brazil

(Dated: September 25, 2017)

Abstract

Purpose: An adequate understanding of bone structural properties is critical for predicting fragility conditions caused by diseases such as osteoporosis, and in gauging the success of fracture prevention treatments. In this work we aim to develop multi-resolution image analysis techniques to extrapolate high-resolution images predictive power to images taken in clinical conditions.

Methods: We performed multifractal analysis (MFA) on a set of 17 *ex-vivo* human vertebræ clinical CT scans. The vertebræfailure loads (F_{Failure}) were experimentally measured. We combined Bone Mineral Density (BMD) with different multifractal dimensions, and BMD with multi-resolution statistics (e.g., skewness, kurtosis) of MFA curves, to obtain linear models to predict F_{Failure}. Furthermore we obtained short- and long-term precisions from simulated in-vivo scans, using a clinical CT scanner. Ground-truth data—high resolution images—was obtained with a High-Resolution Peripheral Quantitative Computed Tomography (HRpQCT) scanner.

Results: At the same level of detail, BMD combined with traditional multifractal descriptors (Lipschitz-Holder exponents), and BMD with monofractal features showed similar prediction powers in predicting F_{Failure}(87%, adj. R2). However, at different levels of details, the prediction power of BMD with multifractal features raises to 92% (adj. R^2) of F_{Failure}. Our main finding is that a simpler but slightly less accurate model, combining BMD and the skewness of the resulting multifractal curves, predicts 90% (adj. R^2) of F_{Failure}.

Conclusions: Compared to monofractal and standard bone measures, multifractal analysis captured key insights in the conditions leading to F_{Failure}. Instead of raw multifractal descriptors, the statistics of multifractal curves can be used in several other contexts, facilitating further research.

* baravalle@cifasis-conicet.gov.ar

† felix.thomsen@uns.edu.ar

‡ cad@uns.edu.ar

§ yongtaolu@dlut.edu.cn

¶ gomez@cifasis-conicet.gov.ar

** borkostosic@gmail.com

†† tastosic@gmail.com

I. INTRODUCTION

Understanding the internal micro-structural properties of bone is critical for monitoring osteoporosis and other related bone diseases. This is especially difficult in trabecular bone of hips and vertebrae, which have rich micro-structures. Previous researches in bone strength assessment have addressed bone bio-mechanical properties [1], the osseus growing process [2, 3], and bone aging [4]. Also, some works applied different technologies in bone imagery acquisitions, such as ultrasound [5]. Other works focused on modeling the different forces acting on the bone structure, to more accurately predict conditions of bone fracture [6, 7].

Some authors proposed methods for characterizing the internal trabecular structure following Euclidean geometry since the 1980s [8, 9]. In the late 1990s, true 3D model independent methods arose [10, 11]. Since then, the focus moved to the accurate estimation of physical entities from blurry in-vivo images. The bone research community extended structural parameters using non-Euclidean fuzzy geometry [12], soft classification approaches [13, 14] or methods based on the fractal dimension [15, 16].

The literature associates bone health with several standard measures [17]. In particular, Bone Mineral Density (BMD) is the most common quantity used to diagnose osteoporosis and other bone health conditions. BMD is able to predict almost 69% (adj. R^2) of the bone failure load [18]. However, combining BMD with other imaging biomarkers, e.g., trabecular thickness or structure model index, has not been able to add significant predictive information to F_{Failure} using High Resolution Quantitative Computed Tomography (HRQCT) [16]. On the other hand, fractal theory can be a valuable tool for feature characterization and analysis of the porous nature of the trabeculae. It allows assessment of several properties such as scale invariance, self-similarity, porosity, rugosity and texture [19]. Monofractals have been successfully applied to analyze bone microstructures [15, 20]. Recent results showed that a model based on BMD with two fractal parameters could explain 89% (adj. R^2) of F_{Failure} under clinical HRQCT resolution [16].

In other image processing contexts, multifractal analysis (MFA) demonstrated to provide robust feature extraction, yielding better classification performances compared with the traditional monofractal approach [21–23]. Nevertheless, so far there are just a few works focused on MFA of osseus' porous structures. Also, most authors implemented it only for 2D images [24, 25]. MFA computes a richer set of descriptors, either in the form of a generalized

dimension function or as a singularity spectrum. MFA intends to extract the entire set of fractal dimensions, assuming that fractal-like objects are a superimposition of distinct fractal sub-structures arising at different spatial scales.

In this work we applied 3D MFA to actual *ex-vivo* trabecular bone images, exploring MFA capabilities together with other parameters in predicting F_{Failure}. Preliminary results in the elaboration of robust linear models predicts 92% (adj. R^2) of the bone F_{Failure} under HRQCT imaging conditions. These results contributes to the most relevant F_{Failure} analysis techniques in the literature [16, 26]. The main contributions of this work are twofold: 1– the demonstration that multifractal analysis of the trabecular bone produces a richer characterization of the mechanical properties with respect to non-fractal and mono-fractal counterparts, and 2– the introduction of a new method for multifractal analysis in multi-resolution bone imagery, which achieves a higher predictive power for fracture risk than previous mono-fractal and non-fractal parameters.

II. MATERIALS AND METHODS

In this section we briefly describe the bone datasets, the mathematical foundations underlying our image analysis techniques, and their computational implementation.

A. Sampled data

We conducted two experiments: The first one to obtain parameter correlations and F_{Failure} prediction models. The second one to determine parameters robustness (short- and long-term precision). The BioAsset consortium [27] produced the first dataset, consisting of 82 *ex-vivo* vertebrae scans from 33 patients who suffered from osteoporosis (81.2 ± 7.1 y). The donors were females aged between 60 and 90, diagnosed with postmenopausal osteoporosis. The diagnosed was made from a T-score of -2.5 or less as assessed by DXA. Each spinal specimen contained three vertebrae T_{11}, T_{12} and L_1 and their intervertebral discs. The vertebrae were scanned with a clinical CT scanner (Siemens Somatom 64, Siemens AG Erlangen, Germany) applying a standard HRQCT protocol (360 mAs, 120 kVp, voxel size $188 \times 188 \times 300 \mu m^3$). Density calibration (mg K_2HPO_4/cm^3) included a calibration phantom (Mindways, Austin TX, USA) underneath the vertebral specimens. After that, vertebrae

were segmented using a Pacman-shaped volume of interest (VOI). The segmentation was performed with a binary threshold at an average bone volume fraction (BV/TV) of 25%. The T_{12} maximum failure load was experimentally collected from a subset of 20 patients. The spinal segments were fixed to a servohydraulic testing machine (Bionix 858.2, MTS Systems, Eden Prairie, MN, USA). Once preconditioned, a quasistatic uniaxial compression (6 mm/min) with a 4 deg flexion angle was applied until middle vertebral body (T_{12}) failed. After excluding those with an insufficient size, seventeen T_{12} vertebrae remained for computing correlations between F_{Failure} and HRQCT parameters. Fig. 1 shows the setup of a failure load measurement and a computational HRQCT representation of the vertebrae highlighting the VOI. We used all 82 vertebrae samples to establish parameter correlations, but only 17 to obtain F_{Failure} linear models.

For the second experiment, we used five human T_{12} vertebral specimens from human cadavers. After removing surrounding soft tissue and marrow the vertebrae were embedded in epoxy resin. The vertebra phantoms were repeatedly scanned on a clinical CT scanner under simulated *in-vivo* conditions. Two protocols, a high-resolution (355 mAs) and a standard resolution (140 mAs) were applied, both with 120 kVp and voxel size $188 \times 188 \times 300 \mu m^3$. Three repetitions were performed with image noise as found under *in-vivo* conditions (abdomen phantom) and two with increased image noise (abdomen phantom with additional body ring). A cylindrical VOI was placed within the trabecular region of all vertebrae, sub-divided into four segments (volume $1.1 - 1.7 cm^3, 1.02 \cdot 10^5 - 1.64 \cdot 10^5$ voxels) and automatically registered between all repeated scans. After applying a normalization of the noise spectrum, using a local micro-structural calibration [28], the segmentation was performed at a threshold with average BV/TV = 25%. For reference purposes, HRpQCT scans of the vertebra phantoms were obtained (XtremeCT I, Osteoporose Praxis Neuer Wall, Hamburg, Germany, standard patient protocol), registered, calibrated and segmented with a threshold with average BV/TV= 10%. Further details of both experiments can be found elsewhere [16, 29].

We obtained the following standard measurements with the software Structural Insight (v3.1, Biomedical Imaging, University of Kiel, Germany) [30]: bone mineral density (BMD) and content (BMC), tissue mineral density (TMD) and content (TMC), total volume (TV), bone volume fraction (BV/TV), bone surface fraction (BS/BV), trabecular number (Tb.N), mean intercept length (MIL), trabecular separation (Tb.Sp) and trabecular

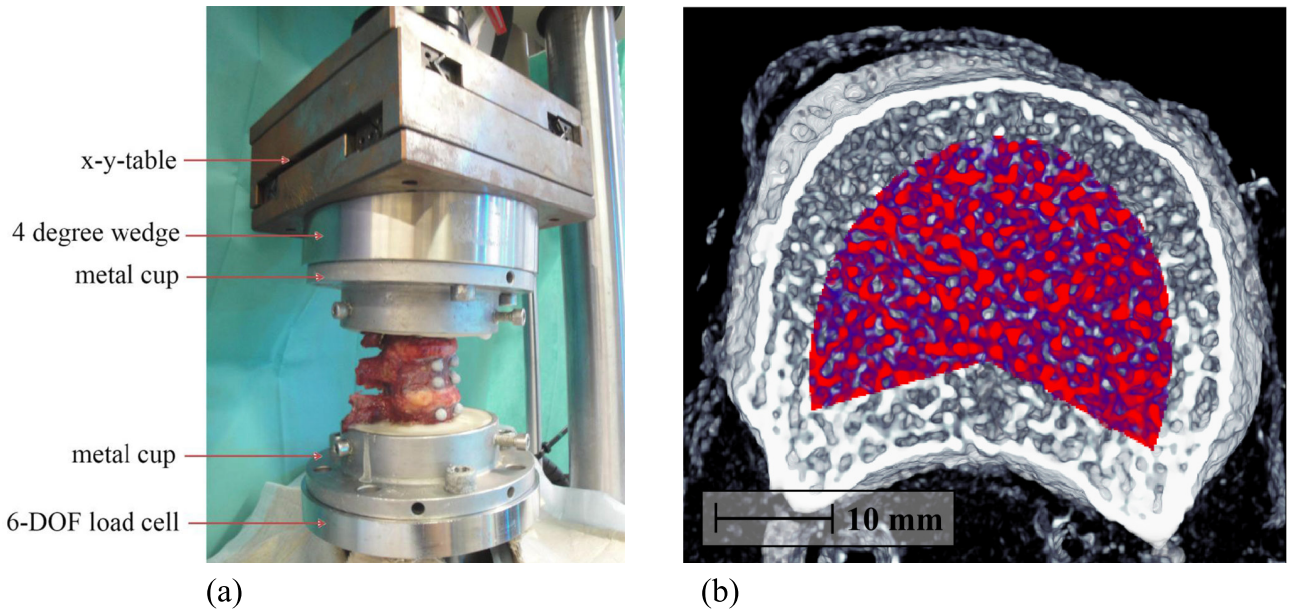

FIG. 1. Human T_{11}-L_1 spinal segment and HRQCT representation of T_{12}. (a) setup for measuring T_{12} vertebra failure load. (b) volume rendering of a HRQCT volume with a Pacman shaped VOI in the spongiosa.

thickness (Tb.Th).

B. Generalized Multifractal Dimension and the Sandbox Method

Fractals are objects characterized by self-similarity under scale changes. One of the most popular methods for fractal image analysis is the *box counting algorithm* that estimates the so called capacity dimension. It can be easily implemented in any underlying embedding space (2D, 3D, etc.). However, natural objects seldom conform to a strict invariability of the monofractal scale. Instead, they should be considered as a *multifractal* hierarchy of many overlapped fractal structures, each with its own scale invariance. Therefore, an adequate characterization of these objects should encompass the multifractal objects underlying complexity. There are two characterizations of this kind that are basically equivalent, namely the *Generalized Multifractal Dimension* and the *Multifractal Singularity Spectrum*.

The Sandbox method is one of the most frequent used methods for computing the generalized multifractal dimensions in the literature, especially in 2D imagery [31–33], and geometrical feature extraction [34].

Fig. 2 (left) shows the generalized multifractal dimensions of a human vertebra that we computed through the sandbox method. In Fig. 2 (left) the multifractal nature of the trabeculæ is quite apparent.

C. Multifractal Spectrum - MFS (Lipschitz-Hölder Exponents)

The MFS is an alternative representation to the generalized dimensions. Both are related by a Legendre transformation. Despite this equivalence, the MFS seems to have a better computational counterpart for image description and classification.

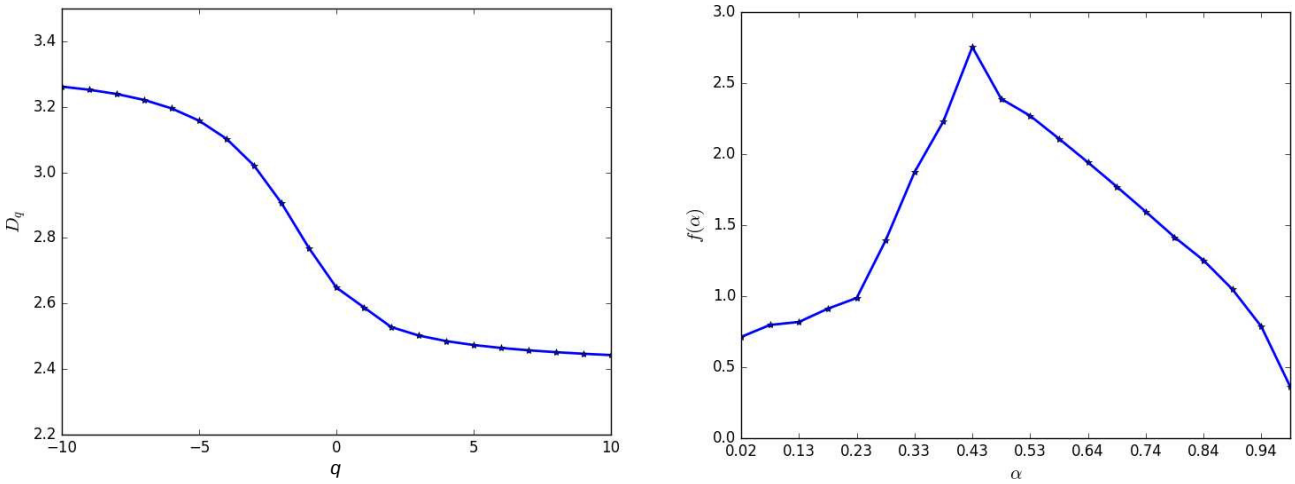

FIG. 2. Three dimensional MFSs of a vertebra HRQCT scan: Sandbox (left) and Lipschitz-Hölder (right) methods. The Figure shows the multifractal nature of vertebrae trabecular tissue.

In addition, it allows to extract more information using measure functions and does not require a prior binarization step. The method can be used to design different features that attend specific purposes, such as robustness to noise or illumination variation [23, 35]. For instance, the energy of the gradients could highlight features that are robust to volume illumination changes (Gradient MFS). Another useful definition is the sum of the Laplacians of the volume (Laplacian MFS). If the input is effectively multifractal, these transformations provide additional meaningful features over the traditional MFS [22].

We implemented a 3D version of the MFS algorithm presented in [23]. Fig. 2 (right) shows this representation. The $f(\alpha)$ values lay between 0.5 and 3 (the disjoint sets can locally look like lines, plates, or solid volumes). As a feature vector, a 3D image MFS produces n pairs $< \alpha, f(\alpha) >$.

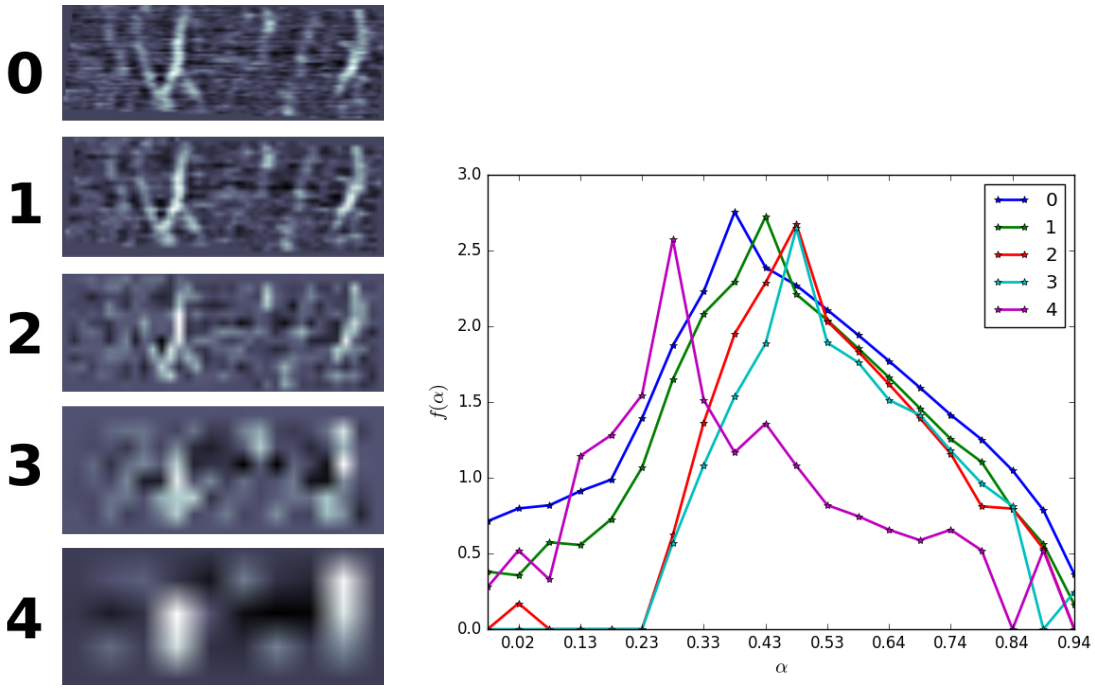

FIG. 3. Pyramid-MFS: 3D volume slices at different levels of detail (0: left, top—unmodified—, 4: left, down—highest downsampling—), and their corresponding MFSs. The resulting feature vector is composed of these 3D MFS ($\text{MFS}_0 \ldots \text{MFS}_4$).

D. Pyramid 3D MFS

The MFS has scale invariance. This means the spectrum features should be—at least statistically—self-similar at different scales. It is possible to perform an analogous multi-resolution analysis considering multiple levels of details through successive low-pass filterings [36, 37]. For this purpose, we computed a pyramid of downsamples successively reducing the 3D image k times to half its size, through trilinear interpolation. Consequently, we obtained a new set of k 3D images with its k MFSs ($\text{MFS}_0 \ldots \text{MFS}_{k-1}$). The resulting feature vector has $n\times$ k elements (where n is the amount of MFS intervals). Fig. 3 shows five successive 3D image downsamples and its respective multifractal spectra. For clarity, the figure shows only one slice. The curves exhibit similarities at different levels of detail. However, when downsampling they differ due to substructure simplifications.

E. Skewness and Kurtosis

In this study, we introduced two multifractal curve features: Skewness (SK)—that measures distribution symmetry [38]—and Kurtosis (KT)—that measures the distribution peak extent—. MFS symmetry indicates whether some sectors have fractal dimension similarities (i.e., structure semblance in the original volume). This becomes critical to identify common substructures that may increase fracture risk. Therefore, we used these features as global descriptors of multifractal distributions.

F. Model Selection Criteria

We combined 3D bone image multifractal analysis with BMD and other classical descriptors of bone health, to improve F_{Failure} predictors. We used several criteria to test linear model combinations. The main model selection criterion is the Robust R^2 score. This indicator uses leave-one-out cross validation scheme (it uses all except one observation to train a model). Then it predicts the left-out observation. Robust R^2 is the result of repeating this process on every observation and taking the prediction score mean. We selected the final models as BMD along with the parameters that obtained a higher Robust R^2 with respect to the actual failure load. We also reported the adjusted R^2s to be compared with other published methods. However, we did not apply it as model selection criterion.

The corrected Akaike Information Criteria (AICc) represents a measure of a model information, with a penalty for model complexity. It is a derivation of the Akaike Information Criteria (AIC) [39], an estimation of a model measure of fit. The AICc results more suitable than the AIC when there are few phenomenon samples. By having AIC, AICc can be computed as [40]

$$AICc = AIC + 2\frac{K(K+1)}{n-K-1}, \tag{1}$$

where K represents number of features and n the observation count.

Based on the AICc, we can compute the p-value or *probabilistic gain of information* of one model over another. Given two linear models M_1 and M_2, if $\text{AICc}_1 < \text{AICc}_2$, then the p-value results

$$p = e^{\frac{AICc_1 - AICc_2}{2}}. \tag{2}$$

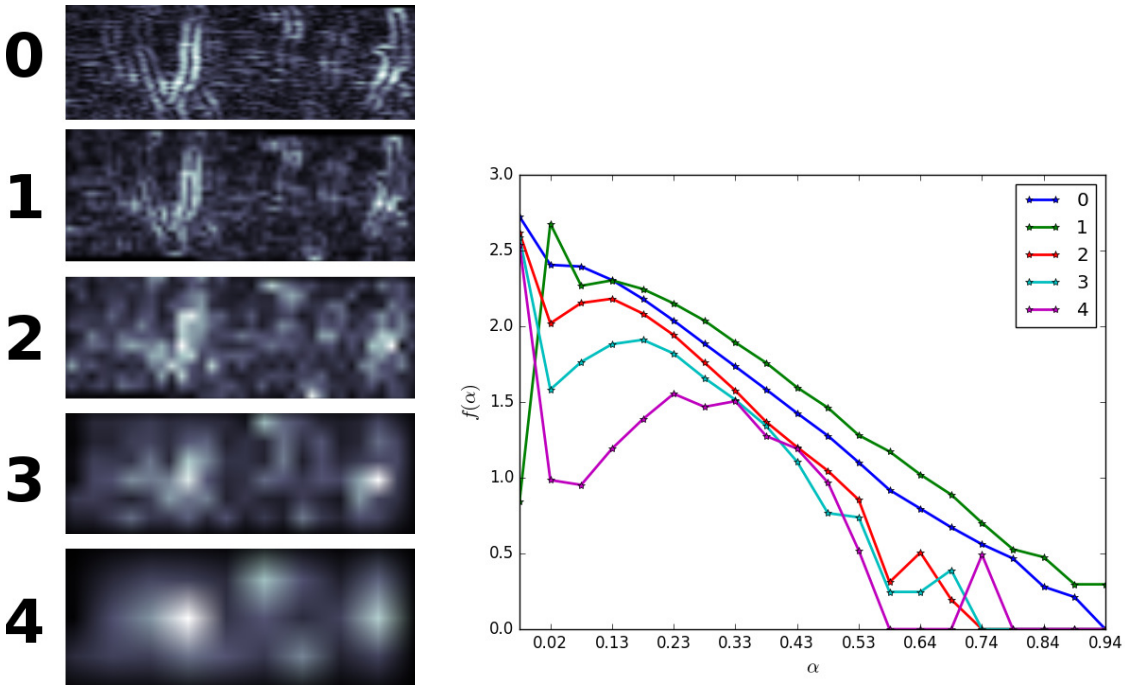

FIG. 4. Pyramid-gradient-MFS: 3D volumes at different levels of detail (0: left, top—unmodified—, 4: left, down—highest downsampling—), and their corresponding gradient MFS. The resulting feature vector is composed of these 3D gradient MFS.

G. Precision and Accuracy

We used normalized short-term-precision (STP) as a precision and repeatability metric, and normalized long-term-precision (LTP), as an accuracy or trueness metric:

$$STP = \sqrt{\frac{\sum_{i=1}^{N}\sum_{j=1}^{M}(x_{ij}-\bar{x}_i)^2}{N(M-1)(\max_i\{\tilde{x}_i\}-\min_i\{\tilde{x}_i\})}}, \tag{3}$$

$$LTP = \sqrt{\frac{\sum_{i=1}^{N}(y_i-\hat{y}_i)^2}{(N-2)(\max_i\{y_i\}-\min_i\{y_i\})}}, \tag{4}$$

where $N = 20$, the number of VOIs, $M = 10$, the number of repeated scans on the VOI, x_{ij} the structural parameter at VOI i and scan j, $\bar{x}$ the arithmetic mean and $\tilde{x}_i$ the median at VOI i, and $\hat{y}_i = a + b\tilde{x}_i$, the linear estimate of $\hat{y}_i$ from the QCT. LTP relates the median $\tilde{x}_i$ at QCT at VOI i with the ground truth HRpQCT (y_i).

H. Correlation coefficients

Since the traditional Pearson coefficient does not assume a linear dependency on the fitted values, in this work we used the Spearman correlation coefficient instead. It was applied to determine similarity between new fractal features and traditional bone measures. This is useful to determine if the fractal features measure new information.

We implemented all presented methods using Python 2.7 and related numerical libraries Scipy (`http://www.scipy.org`), Numpy (`http://www.numpy.org`) and Statsmodel (`http://statsmodels.sourceforge.net/` for linear model fitting).

III. RESULTS

In this section we show the results of applying linear models to predict F_{Failure}. They are grouped in 1-fractal: BMD and MFS features, and 2-standard:BMD and standard parameters. We also tested correlations to assess whether the multifractal features represent new information (i.e., low correlation with standard parameters), and correspondences between multifractal descriptors. Finally, we reproduce precision and accuracy test results.

A. F_{Failure} Linear Models

In Tables I to V, the first row shows BMD predictions of F_{Failure}. Rows 2-4 show the best model (higher Rob.R^2) found combining BMD with one, two or three features. We computed their p-value against the BMD model, representing its statistical information gain. MFS_i subindex (i) indicates the considered level of detail: 0 - input image, 4 - highest downsampling. $\text{MFS}_i[j]$ entry (j) corresponds to the multifractal dimension j.

Table I shows models using standard bone measures. No significant statistical information gain is observed over BMD alone (using up to three parameters, p-value 0.357). Table II shows selected models using the Lipschitz-Hölder exponents. The table shows that MFS explains F_{Failure} with similar accuracy to literature results [16]. With equivalent performance, Table III shows gradient MFS models. Finally, Table IV shows models that combine gradient MFS at different levels of detail, achieving an excellent result without overfitting. However, these models were identified through an exhaustive feature combination search. So we could

not deduce an intuitive interpretation. Fig. 4 shows an example from this method, with resampled volumes and overlapped feature vectors.

TABLE I. Linear model selection using the standard measures for bones.

Model	Features	Adj R^2	Rob. R^2	AICc	p-value	Rob. RMSE
S_1	BMD	0.684	0.634	-0.20	-	0.220
S_2	BMD + TMC	0.756	0.719	-2.26	0.357	0.203
S_3	BMD + BS/BV + MIL	0.762	0.710	0.17	-	0.207
S_4	BMD + TMD + MIL + TMC	0.827	0.774	-1.69	0.475	0.182

TABLE II. Linear model selection using the MFS (Lipschitz-Hölder version) to explain F_{Failure}.

Features	Adj R^2	Rob. R^2	AICc	p-value	Rob. RMSE
BMD	0.684	0.634	-0.20	-	0.220
BMD + $\text{MFS}_0[1]$	0.776	0.742	-4.26	0.129	0.187
BMD + $\text{MFS}_0[0,2]$	0.804	0.795	-4.26	0.129	0.176
BMD + $\text{MFS}_0[0,3,6]$	0.873	0.844	-8.88	0.012*	0.142

TABLE III. Selected models using Gradient MFS.

Features	Adj R^2	Rob. R^2	AICc	p-value	Rob. RMSE
BMD	0.684	0.634	-0.20	-	0.220
BMD + $\text{MFS}_0[8]$	0.816	0.772	-7.56	0.025*	0.169
BMD + $\text{MFS}_0[9,13]$	0.837	0.802	-7.37	0.027*	0.160
BMD + $\text{MFS}_0[3,4,5]$	0.881	0.848	-9.93	0.007*	0.1374

As a more conservative option, in Table V we reproduced selected linear models from Stats-Pyramid-Gradient MFS, i.e., Stats version of the previous model. The table shows that at several levels of detail Skewness faithfully model F_{Failure}.

TABLE IV. Results for the method Pyramid-Gradient MFS. The table shows that some features from the Gradient MFS at different levels provide descriptive approximation of F_{Failure}.

Features	Adj R^2	Rob. R^2	AICc	p-value	Rob. RMSE
BMD	0.684	0.634	-0.20	-	0.220
BMD + $\text{MFS}_0[8]$	0.816	0.772	-7.60	0.025*	0.169
BMD + $\text{MFS}_0[9]$ + $\text{MFS}_1[15]$	0.860	0.820	-9.70	0.009*	0.163
BMD + $\text{MFS}_0[13]$ + $\text{MFS}_1[1]$ + $\text{MFS}_1[18]$	0.924	0.899	-17.56	0.00016*	0.109

TABLE V. Results for the method Stats-Pyramid-Gradient MFS. The (gradient) MFSs' skewness at different levels of detail.

Model	Features	Adj R^2	Rob. R^2	AICc	p-value	Rob. RMSE
	BMD	0.684	0.634	-0.20	-	0.220
F_1	BMD + SK_0	0.845	0.804	-10.50	0.0058*	0.156
F_2	BMD + SK_0 + KT_3	0.870	0.838	-11.20	0.004*	0.143
F_3	BMD + SK_0 + SK_1 + SK_4	0.901	0.856	-13.20	0.0015*	0.124

B. Multifractal vs. Standard models Comparison

To highlight the gain of information, we computed multifractal model p-values over standard versions. Table V last three rows define fractal models F_{1-3}, and Table I standard models S_{1-4}. The simplest fractal linear model (BMD with SK_0) obtains $p(F_1 \text{ vs. } S_{1-4}) = 0.0058^*$ to 0.0162^*. F_2 (BMD with SK_0 and KT_3) gets $p(F_2 \text{ vs. } S_{1-4}) = 0.004^*$ to 0.0114^*. Finally, taking into account the skewness at different levels, $p(F_3 \text{ vs. } S_{1-4}) = 0.0015^*$ to 0.0042^*. Comparisons among fractal models show that F_3 and F_2 are not statistically more significant than F_1, but F_3 predictive capabilities ($Rob.R^2$) suggests it is a more robust predictor of F_{Failure}. These results support the hypothesis that fractal models provide extra information over standard models concerning F_{Failure}.

TABLE VI. Spearman's Correlation Coefficients between multifractal features and Standard measures for bones. $^*p < 0.05$, bold $p < 0.01$ (correlation is significant)

Features	SK_0	SK_1	SK_4	BMD	MIL	Tb.Th	Tb.Sp	BV/TV	Tb.N
SK_1	**0.8996***								
SK_4	0.1576	0.1478							
BMD	-0.2030	**-0.2899***	0.0772						
MIL	-0.1390	-0.1777	-0.0258	**0.352***					
Tb.Th	-0.0642	-0.0800	-0.0240	0.2020	**0.937***				
Tb.Sp	0.0060	0.0056	0.0113	0.1138	**0.8800***	**0.955***			
BV/TV	**-0.2950***	**-0.3100***	-0.0728	**0.2890***	**-0.3550***	**-0.6090***	**-0.7050***		
Tb.N	-0.0465	-0.0362	-0.0186	-0.1064	**-0.8590***	**-0.962***	**-0.9833***	**0.7594***	
F_{Failure}	0.3480	0.0147	0.1862	**0.8382***	0.4700	0.2400	0.2000	0.2500	-0.2000

C. Correlations between MFS and standard parameters

Table VI shows low Spearman correlations coefficients between significant MFS features and standard parameters. This further supports the argument that MFS measures provide new and robust information. Among fractal parameters, only SK_0 is (positively) correlated to SK_1 ($\sim 0.89^*$). F_{Failure} is (positively) correlated only to BMD ($\sim 0.83^*$) and it is not correlated to any fractal parameter.

Fig. 5 shows scatter plots that further explain Spearman correlations found among SK_0, BMD, and F_{Failure}. There is a strong correlation between BMD and F_{Failure} (as shown by the fitting plane), explaining why BMD accounts for a great percentage of failure load. However, skewness does not appear related to other variables.

D. Precision and accuracy

On ten repeated scans, results for main parameters are as follows (STP, LTP): BMC obtained the highest precision and accuracy (6%, 9%), followed by MIL (10%, 7%), BMD

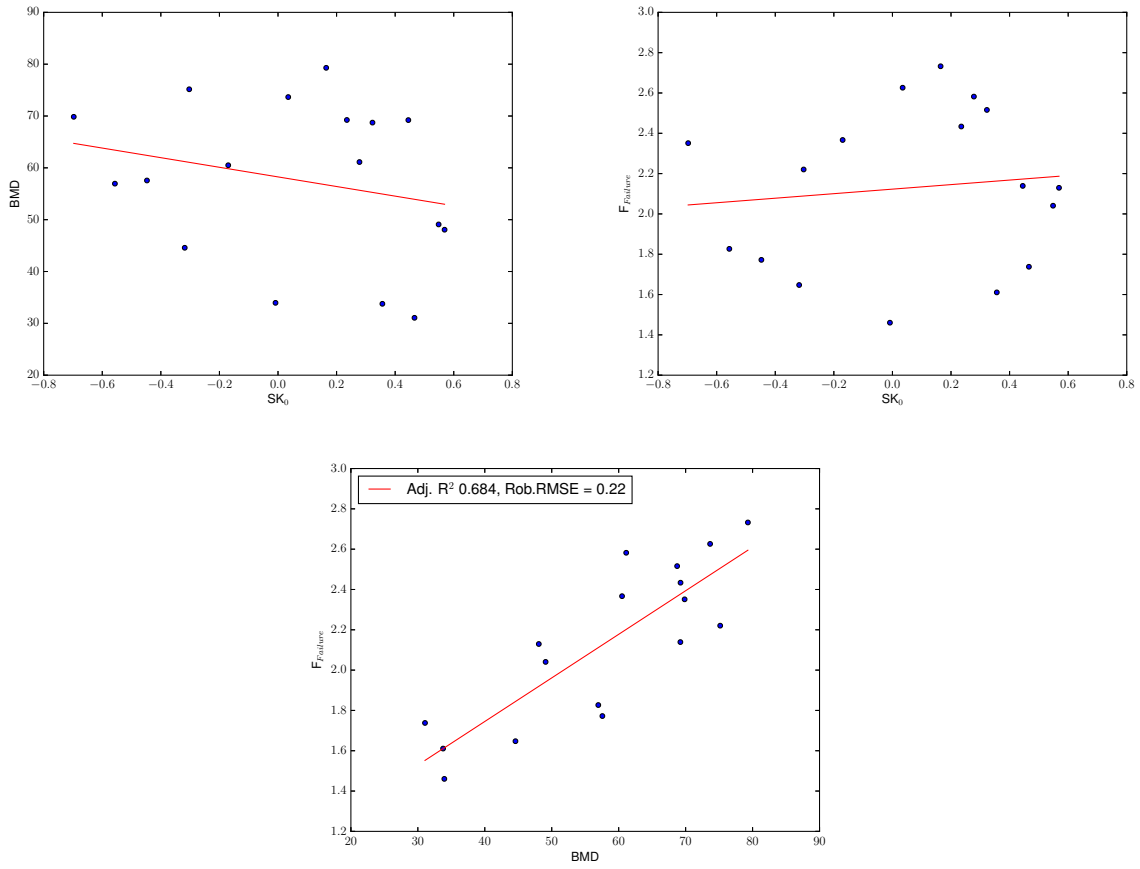

FIG. 5. 2D Scatter plots of the Skewness at downsampling level 0 (SK_0) vs F_{Failure} vs BMD of vertebrae. The plots show strong correlation between BMD and F_{Failure}.

(6%, 13%), Tb.Th: (10%,7%), BS/BV: (10%, 9%), BV/TV (9%, 12%), TMD (19%, 16%), TMC (9%, 21%), Tb.Sp: (11%, 19%), Tb.N: (13%, 20%). Regarding fractal parameters in linear models, SK_0 obtained the most robust values (41%, 22%) followed by SK_1 - SK_4 ($69\% - 82\%$, $23\% - 25\%$), KT_0 (40%, 23%) and KT_1 - KT_4 ($43\% - 63\%$, $27\% - 32\%$).

IV. DISCUSSION

We omitted Sandbox-based linear models which performed worse than BMD only versions. The MFS alone (Lipschitz-Hölder approach, Table II) achieved results comparable to recent literature [16] using up to three parameters (p-value 0.01*). These results agree with feature extraction in the gray level domain, particularly the Trabecular Bone Score (TBS) [41]. Despite this, features represented by raw multifractal dimensions are difficult

to interpret.

In other works [22], authors produced different MFS transforming input data, obtaining features with certain properties such as robustness to noise and illumination changes. Following this, we applied Laplacian and gradient transformations to bone volumes, obtaining modified MFS versions. While Laplacian MFS was not statistical relevant (results not shown for brevity), gradient MFS explained F_{Failure} with similar accuracy to Hölder MFS, and its level of detail version (pyramid-gradient-MFS) increased its accuracy (92%, adj. R^2 of F_{Failure} variability). However, these raw dimensions lack intuitive interpretation, limiting its use as biological markers.

Finally, we derived statistical method versions. The stats-pyramid-gradient-MFS method obtained slightly less predictive power than its non-stats version, but using more intuitive features (e.g., skewness) (Adj.R^2 0.901, Rob.R^2 0.856, AICc -13.2, p-value 0.0015*, Rob.RMSE 0.124)). This means skewness explains more than 90% (Adj.R^2) of F_{Failure} variability at different LOD (more precisely at levels 0, 1, and 4). The best results using only two parameters are given by zeroth level skewness in combination with level 3 kurtosis. Skewness seems to capture the most relevant multifractal information indicating how and/or when the MFS peaks. MFSs' skewness success in explaining F_{Failure} can be attributed to its performance on noisy inputs [42]. These experiments show that multifractal curves statistics summarizes key information of a MFS distribution.

The method can also be defined in 2D, replacing the 3D MFS with the traditional 2D version. Also, it can be extended for use *in-vivo*, with decrease prediction accuracy associated. However, MFS and its variations are common choices for high noise scenarios. Future research should stress this point. Given observed similarities between multifractal curves, skewness models are worth to study in such cases.

We considered only the spongiosa for micro structural feature extraction. Literature shows fracture risk can be determined with high accuracy considering this osseus region only [43, 44]. Precision and accuracy of multifractal parameters, at different levels of detail, are comparable to other state-of-the-art fractal parameters [16]. The lower precision (STP) of newly introduced parameters skewness and kurtosis result most likely from their multi-resolution nature and their statistical characterization as a multifractal curve moment. However, precision might improve in future method versions using alternative skewness and kurtosis definitions—weighted moments, Pearson's skewness coefficients, Bowley skewness—,

or using specifically taylored multifractal distribution statistics. Regarding accuracy (LTP), the most relevant fractal parameters resulted similar to TMC, Tb.Sp, and Tb.N, even in low resolution scenarios (e.g. SK_1). Since we simulated typical clinical *in-vivo* resolutions, our fractal methods are worth being used in human clinical scenarios.

Our work main limitation is the interpretation of multifractal features. While the statistic methods (e.g., skewness) simplify it, further research may find more intuitive fractal features. The models obtained will be useful to define procedural algorithms for bone growing and aging [45], as we did with other porous materials. 3D MFS and its variants can be used in health bone classification.

V. CONCLUSIONS

In this work we extended bone trabecular tissue analysis from fractal to multifractal, and the MFS to 3D. Some contributions include multifractal analysis application to 3D bone images, and a multi-resolution multifractal method with higher failure load predictive power than previous fractal and non-fractal counterparts.

The sandbox-based version obtained worse results than standard measurements methods. However, the MFS method produced features that more precisely predicts F_{Failure}, with surpassing accuracy than current fractal literature. Raw multifractal features were proved to be excellent descriptors (explaining up to 92% in Adj.R^2 of F_{Failure} variability), but their lack of intuitive interpretations may favor the choice of simpler and almost equally descriptive features such as MFS skewness and kurtosis.

Further studies will include CT images analysis with different volume resolutions. We will focus on extending the number of samples and on investigating the influence of X-ray exposure (QCT vs. HQRCT) on fractal properties, obtained through different capture equipments.

ACKNOWLEDGMENT

R. Baravalle and F. Thomsen are both supported by a postdoctoral scholarship of the National Science and Technology Council of Argentina (CONICET). This work was partially supported by grant PGI 24/K061 of SECyT-UNS and by the Chinese Fundamental Research

Funds for the Central Universities - DUT15RC(3)130. We would like to thank Estefanía Hasik for her contribution to improve English readability on this manuscript.

DISCLOSURE OF CONFLICTS OF INTEREST

The authors have no relevant conflicts of interest to disclose.

---

[1] In Gwun Jang and Il Yong Kim. Computational study of wolff's law with trabecular architecture in the human proximal femur using topology optimization. *Journal of Biomechanics*, 41(11):2353 – 2361, 2008.

[2] Hong Wang, Baohua Ji, X Sherry Liu, X Edward Guo, Yonggang Huang, and Keh-Chih Hwang. Analysis of microstructural and mechanical alterations of trabecular bone in a simulated three-dimensional remodeling process. *Journal of biomechanics*, 45(14):2417–2425, 2012.

[3] Y Lu, M Krause, N Bishop, K Sellenschloh, C-C Glüer, K Püschel, M Amling, MM Morlock, and G Huber. The role of patient-mode high-resolution peripheral quantitative computed tomography indices in the prediction of failure strength of the elderly women's thoracic vertebral body. *Osteoporosis International*, 26(1):237–244, 2015.

[4] He Gong, Ming Zhang, Hiu Yan Yeung, and Ling Qin. Regional variations in microstructural properties of vertebral trabeculae with aging. *Journal of bone and mineral metabolism*, 23(2):174–180, 2005.

[5] Frédéric Padilla and Pascal Laugier. Recent developments in trabecular bone characterization using ultrasound. *Current Osteoporosis Reports*, 3(2):64–69, 2005.

[6] Rik Huiskes, Ronald Ruimerman, G Harry Van Lenthe, and Jan D Janssen. Effects of mechanical forces on maintenance and adaptation of form in trabecular bone. *Nature*, 405(6787):704–706, 2000.

[7] Florent Moissenet, Laurence Chèze, and Raphaël Dumas. A 3d lower limb musculoskeletal model for simultaneous estimation of musculo-tendon, joint contact, ligament and bone forces during gait. *Journal of Biomechanics*, 47(1):50 – 58, 2014.

[8] AM Parfitt, CH Mathews, AR Villanueva, M Kleerekoper, B Frame, and DS Rao. Relationships between surface, volume, and thickness of iliac trabecular bone in aging and in osteo-

porosis. implications for the microanatomic and cellular mechanisms of bone loss. *Journal of clinical investigation*, 72(4):1396, 1983.

[9] A. Vesterby, H.J.G. Gundersen, and F. Melsen. Star volume of marrow space and trabeculae of the first lumbar vertebra: Sampling efficiency and biological variation. *Bone*, 10(1):7 – 13, 1989.

[10] Tor Hildebrand and Peter Rüegsegger. Quantification of bone microarchitecture with the structure model index. *Computer Methods in Biomechanics and Biomedical Engineering*, 1(1):15–23, 1997.

[11] Tor Hildebrand and Peter Rüegsegger. A new method for the model-independent assessment of thickness in three-dimensional images. *Journal of Microscopy*, 185(1):67–75, 1997.

[12] A. Darabi, F. Chandelier and G. Baroud. Thickness analysis and reconstruction of trabecular bone and bone substitute microstructure based on fuzzy distance map using both ridge and thinning skeletonization *Canadian Journal of Electrical and Computer Engineering*, 34(1-2):57–62, 2009.

[13] Rodrigo Moreno, Örjan Smedby and Magnus Borga. Soft classification of trabeculae in trabecular bone In *2011 8th IEEE International Symposium on Biomedical Imaging (ISBI)*, pages 1641–1644, May 2011.

[14] Punam K Saha, Yinxiao Liu, Cheng Chen, Dakai Jin, Elena M Letuchy, Ziyue Xu, Ryan E Amelon, Trudy L Burns, James C Torner, Steven M Levy, et al. Characterization of trabecular bone plate-rod microarchitecture using multirow detector ct and the tensor scale: Algorithms, validation, and applications to pilot human studies. *Medical physics*, 42(9):5410–5425, 2015.

[15] Laurent Pothuaud, Pascal Carceller, and Didier Hans. Correlations between grey-level variations in 2D projection images (TBS) and 3D microarchitecture: applications in the study of human trabecular bone microarchitecture. *Bone*, 42(4):775–787, 2008.

[16] Felix Thomsen, Jaime Peña, Yongtao Lu, Gerd Huber, Michael Morlock, Claus-C. Glüer, and Claudio Delrieux. A new algorithm for estimating the rod volume fraction and the trabecular thickness from in vivo computed tomography. *Medical Physics*, 43(12):6598–6607, 2016.

[17] Elisabeth APM Romme, Erica Rutten, Piet Geusens, Joost JA de Jong, Bert van Rietbergen, Frank WJM Smeenk, Emiel FM Wouters, and Joop PW van den Bergh. Bone stiffness and failure load are related with clinical parameters in men with chronic obstructive pulmonary disease. *Journal of Bone and Mineral Research*, 28(10):2186–2193, 2013.

[18] Julien Wegrzyn, Jean-Paul Roux, Monique E Arlot, Stéphanie Boutroy, Nicolas Vilayphiou, Olivier Guyen, Pierre D Delmas, Roland Chapurlat, and Mary L Bouxsein. Role of trabecular microarchitecture and its heterogeneity parameters in the mechanical behavior of ex vivo human L3 vertebrae. *Journal of Bone and Mineral Research*, 25(11):2324–2331, 2010.

[19] Benoit B. Mandelbrot. *The fractal geometry of nature*. W.H. Freeman, New York, 1 edition, August 1982.

[20] R. Lopes, P. Dubois, I. Bhouri, M.H. Bedoui, S. Maouche, and N. Betrouni. Local fractal and multifractal features for volumic texture characterization. *Pattern Recognition*, 44(8):1690 – 1697, 2011.

[21] Jelena Andjelkovic, Natasa Zivic, Branimir Reljin, Vladimir Celebic, and Iva Salom. Application of multifractal analysis on medical images. *Wseas Transactions on Information Science and Applications*, 5(11):1561–1572, 2008.

[22] Rodrigo Baravalle, Claudio Delrieux, and Juan Carlos Gómez. Multifractal characterisation and classification of bread crumb digital images. *EURASIP Journal on Image and Video Processing*, 2015(1):9, 2015.

[23] Yong Xu, Hui Ji, and Cornelia Fermüller. Viewpoint invariant texture description using fractal analysis. *Int. J. Comput. Vision*, 83(1):85–100, June 2009.

[24] Philip Caligiuri, Maryellen L Giger, and Murray Favus. Multifractal radiographic analysis of osteoporosis. *Medical physics*, 21(4):503–508, 1994.

[25] Jelena Vasiljevic, Branimir Reljin, Jelena Sopta, Vesna Mijucic, Goran Tulic, and Irini Reljin. Application of multifractal analysis on microscopic images in the classification of metastatic bone disease. *Biomedical microdevices*, 14(3):541–548, 2012.

[26] Yongtao Lu, M Krause, N Bishop, K Sellenschloh, Claus-C. Glüer, K Püschel, M Amling, MM Morlock, and G Huber. The role of patient-mode high-resolution peripheral quantitative computed tomography indices in the prediction of failure strength of the elderly women's thoracic vertebral body. *Osteoporosis International*, 26(1):237–244, 2015.

[27] Claus-C Glüer, Matthias Krause, Oleg Museyko, Birgit Wulff, Graeme Campbell, Timo Damm, Melanie Daugschies, Gerd Huber, Yongtao Lu, Jaime Peña, et al. New horizons for the in vivo assessment of major aspects of bone quality microstructure and material properties assessed by quantitative computed tomography and quantitative ultrasound methods developed by the bioasset consortium. *Osteologie*, 22(3):223–233, 2013.

[28] Felix Thomsen. Medical 3D image processing applied to computed tomography and magnetic resonance imaging. *Universidad Nacional del Sur*, PhD thesis, 2017.

[29] Yongtao Lu, Ghislain Maquer, Oleg Museyko, Klaus Püschel, Klaus Engelke, Philippe Zysset, Michael Morlock, and Gerd Huber. Finite element analyses of human vertebral bodies embedded in polymethylmethalcrylate or loaded via the hyperelastic intervertebral disc models provide equivalent predictions of experimental strength. *Journal of Biomechanics*, 47(10):2512–2516, 2014.

[30] Felix Thomsen, Jaime Peña, Claudio Delrieux, and Claus-Christian Glüer. Structural Insight v3: A stand-alone program for micro structural analysis of computed tomography volumes. In *Anales del Congreso Argentino de Informática y Salud*, September 2016.

[31] Tamás Tél, Ágnes Fülöp, and Tamás Vicsek. Determination of fractal dimensions for geometrical multifractals. *Physica A: Statistical Mechanics and its Applications*, 159(2):155 – 166, 1989.

[32] Samuele G. De Bartolo, Roberto Gaudio, and Salvatore Gabriele. Multifractal analysis of river networks: Sandbox approach. *Water Resources Research*, 40(2), 2004.

[33] T. Stosic and B. D. Stosic. Multifractal analysis of human retinal vessels. *IEEE Transactions on Medical Imaging*, 25(8):1101–1107, Aug 2006.

[34] Ursula Gonzales-Barron and Francis Butler. Fractal texture analysis of bread crumb digital images. *European Food Research and Technology*, 226:721–729, 2008.

[35] B. B. Mandelbrot. Multifractal measures, especially for the geophysicist. *Pure and Applied Geophysics*, 131:5–42, March 1989.

[36] Yong Xu, SiBin Huang, Hui Ji, and Cornelia Fermuller. Combining powerful local and global statistics for texture description. In *Computer Vision and Pattern Recognition, 2009. CVPR 2009. IEEE Conference on*, pages 573–580. IEEE, 2009.

[37] Yong Xu, Sibin Huang, Hui Ji, and Cornelia Fermüller. Scale-space texture description on sift-like textons. *Computer Vision and Image Understanding*, 116(9):999 – 1013, 2012.

[38] D. Zwillinger and S. Kokoska. *CRC standard probability and statistics tables and formulae*. CRC, 1999.

[39] H. Akaike. A new look at the statistical model identification. *IEEE Transactions on Automatic Control*, 19(6):716–723, Dec 1974.

[40] Kenneth P. Burnham and David R. (biologiste) Anderson. *Model selection and multimodel inference : a practical information-theoretic approach*. Springer, New York, 2002.

[41] Barbara C Silva, William D Leslie, Heinrich Resch, Olivier Lamy, Olga Lesnyak, Neil Binkley, Eugene V McCloskey, John A Kanis, and John P Bilezikian. Trabecular bone score: a noninvasive analytical method based upon the dxa image. *Journal of Bone and Mineral Research*, 29(3):518–530, 2014.

[42] Lorenzo Rimoldini. Weighted skewness and kurtosis unbiased by sample size and gaussian uncertainties. *Astronomy and Computing*, 5:1 – 8, 2014.

[43] Amira I Hussein and Elise F Morgan. The effect of intravertebral heterogeneity in microstructure on vertebral strength and failure patterns. *Osteoporosis International*, 24(3):979–989, 2013.

[44] Ara Nazarian, Martin Stauber, David Zurakowski, Brian D. Snyder, and Ralph Müller. The interaction of microstructure and volume fraction in predicting failure in cancellous bone. *Bone*, 39(6):1196 – 1202, 2006.

[45] Rodrigo Baravalle, Leonardo Scandolo, Claudio Delrieux, Cristian García Bauza, and Elmar Eisemann. Realistic modeling of porous materials. *Computer Animation and Virtual Worlds*, 28(2):e1719–n/a, 2017. e1719 cav.1719.